Materials Research Bulletin 73 (2016) 394–400

Contents lists available at ScienceDirect

Materials Research Bulletin

journal homepage: www.elsevier.com/locate/matresbu

Enhanced electrochemical performances of silicon nanotube bundles anode coated with graphene layers

Jingjing Chen[a,b], Lijian Bie[b], Jing Sun[a], Fangfang Xu[a,*]

[a] State Key Laboratory of High Performance Ceramics and Superfine Microstructures, Shanghai Institute of Ceramics, Chinese Academy of Sciences, Shanghai 200050, PR China
[b] School of Materials Science and Engineering, Tianjin University of Technology, Tianjin 300384, PR China

ARTICLE INFO

Article history:
Received 10 March 2015
Received in revised form 21 September 2015
Accepted 23 September 2015
Available online 28 September 2015

Keywords:
A: Inorganic compounds
A: Nanostructures
B: Microstructure
B: Chemical synthesis
D: Electrochemical properties

ABSTRACT

Significant enhancement in electrochemical performances has been achieved in silicon nanotube bundles (Si NBs) via coating with graphene layers (denoted as Si NBs@G), which could be a promising anode material in Li-ions batteries. The synthesized Si NBs@G have tubular structure with a diameter of around 200 nm and a thickness about 80 nm and the tube walls are composed of Si nanocrystals with a size about several nanometers. Galvanostatic charge-discharge measurements showed that the Si NBs@G displayed gradual increasing in capacity after first 100 cycles and finally reached a capacity of ~765 mAh g^{-1} at 600 cycles, which was almost fivefold the capacity of the parent Si NBs without graphene coating. The graphene outerlayer is considered to serve as the mechanical protecting layer to enhance structural sustainability of Si NBs anode by forming stable solid electrolyte interface. In addition, the formation of Li-rich $Li_{15}Si_4$ crystallites also contributes to the capacity improvement.

1. Introduction

Battery demands for transport and grid applications are expected to be boosted in the years to come [1]. Of all batteries, high energy lithium ion batteries are promising for consumer electronics, electric-drive vehicles and grid-scale stationary energy storage [2]. Silicon has been considered to be an attractive alloy-type anode material because of its highest known theoretical capacity of 4200 mAh g^{-1} with the formation of $Li_{4.4}Si$ alloy [3], which is ten times higher than that of traditional graphite anode [4]. Unfortunately, utilization of silicon-containing anode materials for lithium-ion batteries is usually limited by manufacturing cost, their intrinsic low electric conductivity, and serious volume changes during cycling [5]. In recent years, various approaches have been employed to overcome the limitations of silicon materials. Nanostructured silicon ranging from nanowires, nanofilms, nanotubes to nanoparticles and their composites, in which the strain can be relaxed easily without mechanical fracture because of their smaller size and available surrounding free spaces, have been exploited widely to alleviate the structure deterioration efficiently [6–10]. Si nanotube bundles (NBs) have been successfully synthesized at large scale in our previous work [11] via a magnesiothermic reduction method [12]. However, structural collapse still occurred during prolonged electrochemical reactions for these long Si tubes with length larger than several micrometers, hence resulting in unsatisfactory electrochemical performances. Recent work by Wu et al. developed a smart way to preserve the low dimensional morphology of Si via coating the tubes with amorphous SiO_2 layer, which served as a mechanical protecting layer helping to form stable solid electrolyte interphase (SEI), thus giving rise to better cycle performance [13].

In the present study, strong and Li acceptable graphene layers were coated on Si NBs aiming to improve the structural sustainability and electrochemical performances. X-ray diffractometry (XRD), Raman spectrometry, scanning electron microscopy (SEM) and Transmission Electron Microscopy (TEM) were employed to investigate the structure and morphology of the as-prepared Si NBs@G as well as the structural evolution after cycling in cell. Electrochemical performances of Si NBs@G served as anode materials were investigated with comparison to the parent Si NBs.

2. Experimental

2.1. Sample preparation

The synthetic processes of Si NBs@G were illustrated schematically in Fig. 1. We used the hydroxylapaptite ($Ca_{10}(PO_4)_6(OH)_2$, HAP) nanobelt bundles as sacrificial templates, which were

* Corresponding authors.
E-mail addresses: jingsun@mail.sic.ac.cn (J. Sun), ffxu@mail.sic.ac.cn (F. Xu).

http://dx.doi.org/10.1016/j.materresbull.2015.09.028
0025-5408/

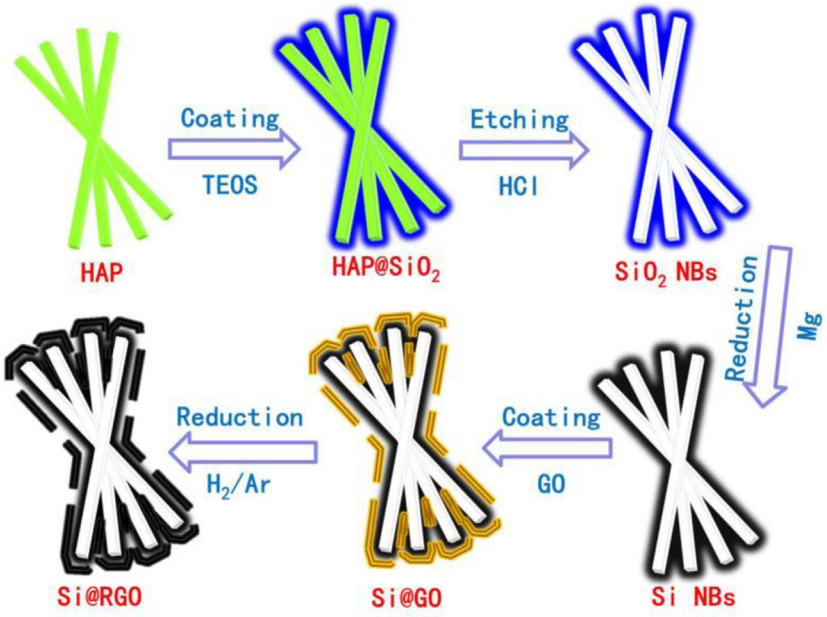

Fig. 1. Schematic illustration of the synthetic routes for Si NBs@G. HAP NBs were used as sacrificial templates, then silica was coated on the HAP NBs to form HAP@SiO_2. SiO_2 NBs were obtained after etching of HAP NBs, magnesiothermic reduction was then applied to convert SiO_2 NBs to Si NBs. on Si NBs. Finally, graphene oxide layers were coated on Si NBs and reduced to from Si NBs@G.

prepared by a hydrothermal method. Then silica was coated on the HAP NBs(indexed as HAP@SiO_2). After etching of HAP cores by HCl solution, SiO_2 NBs were obtained, followed by a magnesiothermic reduction (using Mg metals as reductant) to convert SiO_2 NBs to Si NBs. Si NBs were then treated with (3-aminopropyl)-triethoxysilane (APTES) to fabricate graphene oxide layers on Si NBs. Finally, graphene layers coated Si NBs can be obtained after reduction treatment using H_2/Ar. The experimental details of each step were described as following.

Details of synthesis of Si NBs have been reported elsewhere[11]. Typically, HAP nanobelt bundles were prepared by adding $NaH_2PO_4{\cdot}H_2O$ and $CaCl_2$ one after another to the solution composed of polyethyleneimine, maleic acid and urea, followed by thermal treatment at 120 °C for 2 days. HAP@SiO_2 core–shell composites were synthesized using tetraethoxysilane (TEOS) as source material. After removing the HAP template by 1 M HCl solution, the as-obtained SiO_2 NBs were finally converted to Si NBs through magnesiothermic reduction at 650 °C for 2 h using magnesium powders (molar ratio of Mg to Si was 2:1).

The graphene oxide (GO) was prepared by a modified Hummers method[14]. 1 g graphite powders and 0.8 g $NaNO_3$ were added to 23 mL concentrated H_2SO_4. Then, 3 g $KMnO_4$ was added gradually with stirring in an ice–water bath and the mixture was further stirred at room temperature for 5 days. The solution was diluted by 200 mL distilled water, during which the temperature of the solution was increased up to 98 °C. After staying for 15 min, 10 mL of 30% H_2O_2 was added to the solution, leading to the formation of GO plates. The products were then centrifuged and washed with 5% HCl solution, distilled water and ethanol for several times. Finally, the dark brown GO plates were dispersed in ethanol for further use.

APTES was used as coupling reagent for the fabrication of graphene layers on Si NBs according to others references [15,16]. Si NBs (0.2 g) and APTES (2 mL) were mixed in ethanol (30 mL) and stirred overnight. After filtration, the pretreated Si NBs were mixed with certain amount of GO solution (mass ratio Si: GO = 1:0.3) in ethanol under ultrasound and stirring at room temperature for 3 h. Thereafter, the mixed solution was transferred to an agate mortar placed on an 80 °C heating platform. The moderate heating associated with gentle lapping using an agate pestle could eventually remove the ethanol in the solution, and thus Si NBs@GO powders were obtained. Finally, the Si NBs@GO was reduced by Ar/H_2 gas (600 °C overnight) to form Si NBs @G.

2.2. Structural and morphological characterization

The crystal structure and the phase purity of as-prepared Si NBs and Si NBs@G samples were examined using powder X-ray diffractometer (XRD Ultima IV) with $Cu_{K\alpha}$ radiation operating at 40 kV and 40 mA. Raman spectrum was obtained using a THERMO FISHER DXR micro-Raman spectrometer with an excitation wavelength of 532 nm. Microstructures were measured by TEM (JEOL 2100F) and SEM (Hitachi S4800) both equipped with Oxford energy disperse spectroscopy (EDS) system. FEI Tecnai G2 F20 TEM equipped with a Gatan Enfina spectrometer was used to perform electron energy-loss spectrometry (EELS) analysis.

2.3. Electrochemical evaluations

The electrodes were prepared by mixing of Si NBs@G active material, acetylene black and polyvinylidene fluride (PVDF) binder (the mass ratio was 7:2:1) to form slurry in *N*-methyl-2-pyrrolidone (NMP). The slurry was then cast on a Cu foil and a doctor blade with a gap opening of 120 μm was used to define the maximum thickness of the casted layer. The film was dried at 80 °C in vacuum, followed by compressing under 10 MPa pressure before assembling. The cells were assembled in an argon-filled glovebox with the concentrations of moisture and oxygen below 1 ppm. The electrolyte used was 1 M $LiPF_6$ in a 50:50 mass ratio ethylene carbonate (EC):dimethyl carbonate (DMC) solvent. Electrochemical investigations were conducted using a CT 2001 battery tester. Cyclic voltammetry (CV) was carried out in a voltage range of 0–1.5 V with a scan rate of 0.5 mV s^{-1}. All of the electrochemical

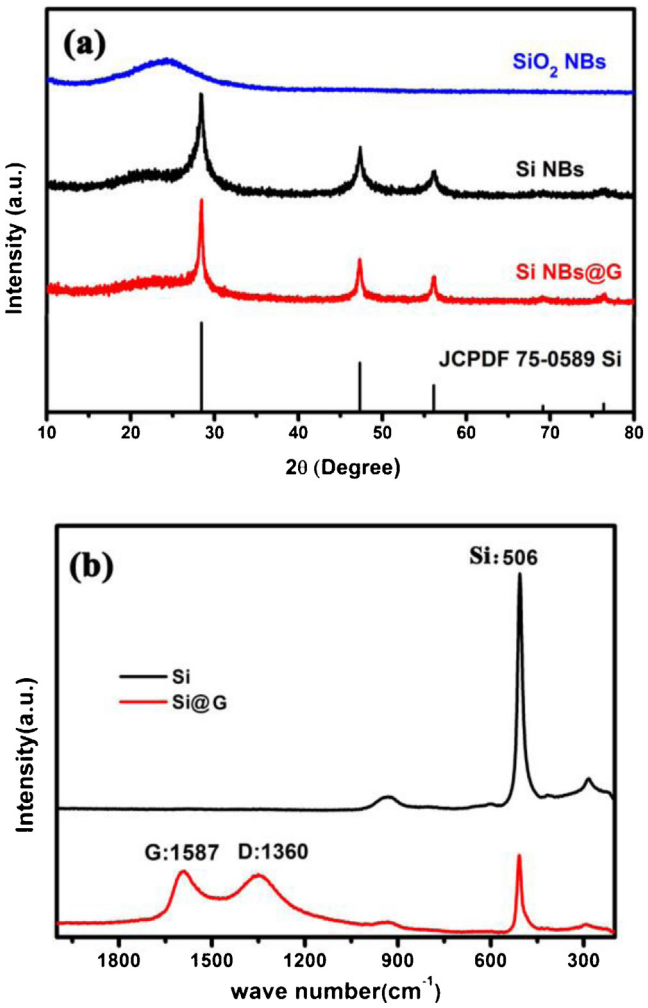

Fig. 2. (a) XRD patterns of SiO_2 NBs, Si NBs and Si NBs@G samples. (b) Raman spectra of Si NBs and Si NBs@G. Both XRD and Raman examination exhibit sharp Si peaks indicative of well crystallized Si in Si NBs and Si NBs@G samples. XRD pattern of Si NBs@G shows narrower peak width of crystalline Si compared with that of Si NBs and lower band of amorphous SiO_2. The two broad peaks on the Raman spectra at 1348 cm^{-1} and 1601 cm^{-1} refer to the first-order D and G peaks of graphene, respectively.

properties of the electrodes were characterized at room temperature. Li foil was used as the counter electrode. For comparison, Si NBs without graphene layers were also encapsulated into coin cells for electrochemical property measurement. Electrodes after certain rounds of cycling were again characterized by TEM and Raman after being taken out of the cell in the glovebox and rinsed with DMC.

3. Results and discussion

Both XRD (Fig. 2(a)) and Raman (Fig. 2(b)) examination exhibit sharp Si peaks indicative of well crystallized Si in Si NBs and Si NBs@G samples. On the Raman spectra, the two broad peaks at 1348 cm^{-1} and 1601 cm^{-1} refer to the first-order D and G peaks of graphene, respectively. XRD pattern of Si NBs@G shows lower band of amorphous SiO_2 and narrower peak width of crystalline Si compared with that of Si NBs. Slight enhancement of Si crystallization should be ascribed to the additional reduction process and annealing effect during the reduction of graphene oxide in Ar/H_2 atmosphere at 600 °C. TEM and SEM observations (Fig. 3) clearly evidence the successful mounting of graphene layers onto the Si NBs. SiO_2 NBs have a diameter of around 200 nm and a thickness about 80 nm. The Si NBs inherit the tubular structure (Fig. 3b) and the tube walls are composed of Si nanocrystals with a size about several nanometers (Fig. 3c).

Electrochemical properties of Si NBs and Si NBs@G anodes have been evaluated using galvanostatic charge/discharge cycling from 1.5 to 0 V at 200 mA g^{-1} in coin-type cells. In comparison with Si NBs, Si NBs@G exhibit a remarkable improvement in term of specific capacity and cycling stability. As can be seen in Fig. 4(a), the first discharge capacity (abbreviation, DCC) and charge capacity (abbreviation, CC) for Si NBs electrode were 1844 and 1044 mAh g^{-1}, respectively. The coulombic efficiency (abbreviation, CE) was then evaluated to be 56.6%. For the Si NBs@G, the first DCC and CCs were 1558 and 906 mAh g^{-1}, respectively, indicating a CE of 58.1%. Lower DCC and CC for the Si NBs material at the first cycle might be ascribed to the larger proportion formation of SEI. However, better mechanical property of graphene layers favor the interconnection of Si crystalline particles upon expansion/contraction in a charge/discharge process, giving a higher 1st CE for Si NBs@G.

Although both the Si NBs and Si NBs@G electrodes exhibit evident fading of discharge capacity in the first 100 cycles, the capacity of Si NBs@G electrode gradually increased afterwards. The capacity decreasing in the incipient cycles was ascribed to the SEI formation (a possible reaction between Li^+ from the electrolyte and residual SiO_2 in Si NBs due to the incomplete magnesiothermic reduction). During lithiation, the Si can be lithiated into a phase with low lithium content, which is one of the reason for the capacity decrease in the first several cycles [17]. The decrease of capacity tends to slow down after 20 cycles for Si NBs@G and eventually gives a minimum capacity of ~320 mAh g^{-1} at about 100th cycle, which is nearly twice the value for Si NBs at this stage. The mild decrease of capacity for Si NBs@G undoubtedly owes to the existence of graphene coating, which serves as the mechanical protecting layers to restrain the pulverization of silicon anode. In the following cycles, the capacity becomes stable at a low value for the Si NBs anode (Fig. 4(b)), while the Si NBs@G on the contrary exhibits a gradual increase in capacity which finally reaches to 765 mAh g^{-1} after 600 cycles (Fig. 4(c)), almost fivefold the capacity (~150 mAh g^{-1} after 600 cycles) of Si NBs (see Fig. 4(a)). Increase in capacity at later cycles has also been reported in other carbon coated anode materials [18,19], however, the reason remains unknown. The graphene or other carbon layers may have important influences on this.

Cyclic voltammetry measurements have been carried out to characterize the redox reactions during charge/discharge cycles of Si NBs (Fig. 4(d)) and Si NBs@G (Fig. 4(e)) anode materials. It was well recognized that the reduction peak at the range 0.6–0.8 V versus Li/Li^+ corresponds to the formation of SEI layers on the surface of Si active materials [20]. Compared to that of Si NBs (Fig. 4(d)), the CV curve of Si NBs@G (Fig. 4(e)) displays a smaller peak in this voltage range and lower current, indicating that the graphene layer wrapping on the Si NBs strengthens the contact with the electrolyte, resulting in less SEI formation and smaller irreversible capacity [21]. Graphene wrapping on the silicon can to some extent hinder the transportation of Li+. Besides, the graphene we used was prepared by Hummers method. Graphite was oxidized then exfoliated to form graphene oxide. Graphene achieved by reduction of graphene oxide contains lots of defects thus has lower current. A broad reduction process between 0.1–0.3 V (vs. Li/Li^+) on the charging curve refers to the Li-alloying process, see eq. (1). The two oxidation peaks, located between 0.38 and 0.60 V, are assigned to the Li-dealloying process (eq. (2)), corresponding to different delithiation degrees of a-$Li_{x'+x''}Si$ into a-$Li_{x'}Si$ and a-Si, respectively [22]. No significant peaks related to

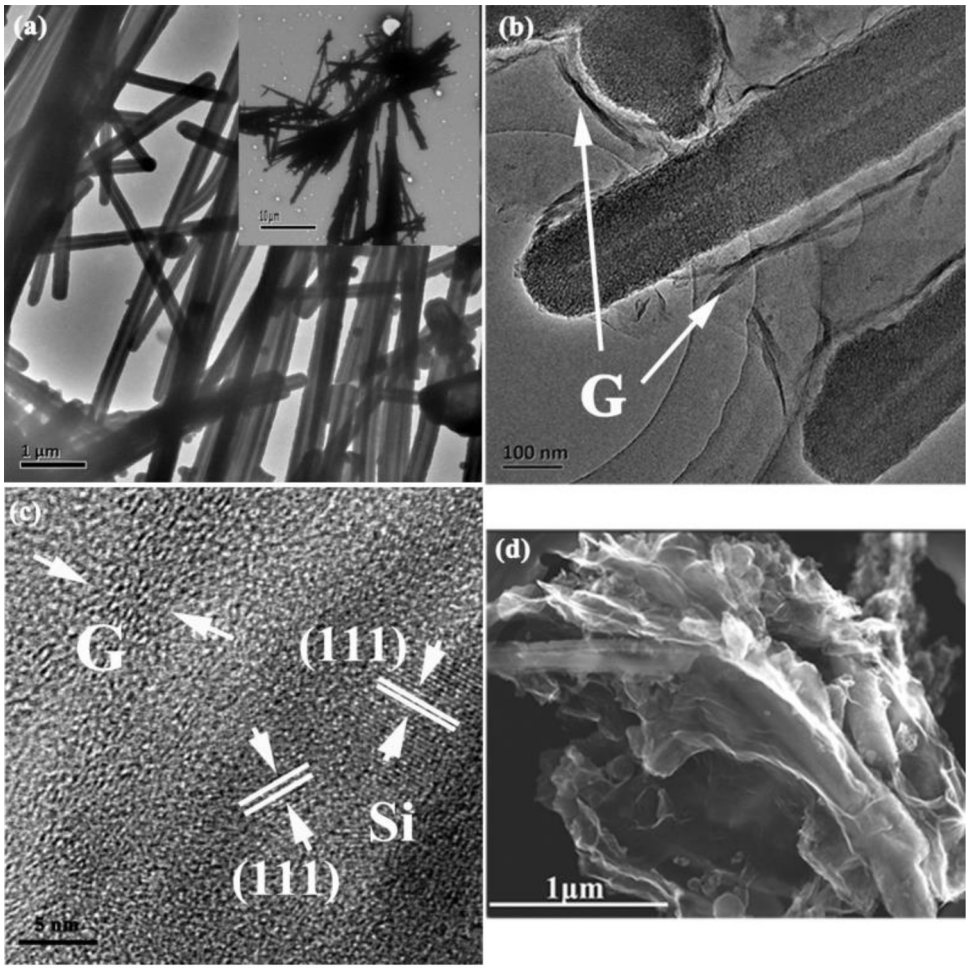

Fig. 3. TEM image of (a) SiO_2 NBs, and (b) Si NBs@G; Inset of Fig. 3a is lower magnification figure of SiO_2 NBs. SiO_2 NBs have a diameter of around 200 nm and a thickness about 80 nm. The Si NBs inherit the tubular structure and the tube walls are composed of Si nanocrystals with a size about several nanometers. (c): high resolution TEM image of Si NBs@G; we can see both the graphene layers and the nano-crystal Si. (d): SEM image of Si NBs@G. Si was wrapped with graphene.

graphene can be observed in Fig. 4(e), suggesting the redox behavior is dominated by the inner Si NBs rather than the graphene coating layers.

$$\text{Lithiation}: \ \mathrm{Si(c)} + x\mathrm{Li}^+ + x\mathrm{e}^- \rightarrow \mathrm{Li}_x\mathrm{Si(a)}$$

$$\text{Delithiation}: \ \mathrm{Li}_x\mathrm{Si(a)} \rightarrow \mathrm{Si(a)} + x\mathrm{Li}^+ + x\mathrm{e}^- \quad (2)$$

where c = crystal and a = amorphous.

Structural pulverization during the repeated charge/discharge processes is the main reason for the failure of cycling stability of Si anodes [23]. In order to evaluate the effectiveness of graphene holding layers in minimizing the structural collapse, the anode materials have been re-collected for characterization after electrochemical cycling in cells. Raman spectrum of the Si NBs@G sample illustrates weakening of the peak (at ~516 cm^{-1}) characteristic of crystallized silicon after the 7th cycle in alloying state, evidencing an almost complete lithiation process (see eq (1)) where crystallized Si has converted to amorphous Li_xSi. The sharp peak of crystallized silicon finally disappears after the 90th cycle in its dealloying state, indicating that amorphous Si rather than crystalline Si is formed in the delithiation process (see eq (2)). On the background, the existing of SiO_2 peak after the 90th cycle suggests no or incomplete reaction happened during these cycles. The G and D peaks of graphene layer in alloying state at the 7th cycle (the red line in Fig. 5) are slightly right shifted, suggesting that the lithiation process has also taken place in the graphene layers during cycling. The insertion of Li^+ expands the interlayer spacing of graphene and thus decreases the atomic vibration frequency, giving rise to shift of Raman peaks to the lower frequency range.

Structural evolution after charge/discharge cycles have been examined by TEM (see Fig. 6). After ten cycles, Si NBs samples exhibit specific double-shell tubular morphology (Fig. 6(a)). Given the crystalline silicon would transform to amorphous during cycling[24–26], the selected area electron diffraction (SAED) still shows polycrystalline reflections of silicon, indicating an incomplete lithiation process (Fig. 6(b)).

Poor electrical transport due to larger amount of residual SiO_2 may allow only small depth of Si NBs surface area to involve in the charge/discharge process. Dilatation of outer reaction region makes itself detached from the inner area, leaving a gap in-between them. Therefore, it seems that only a small portion of Si NBs have taken part in the electrochemical process, hence a small effective mass of active materials. Moreover, the hollow gaps between the double shells would hinder the transport of Li^+ ions during the charge/discharge process, which further impedes the capacity increasing of Si NBs. On the contrary, the Si NBs@G shows

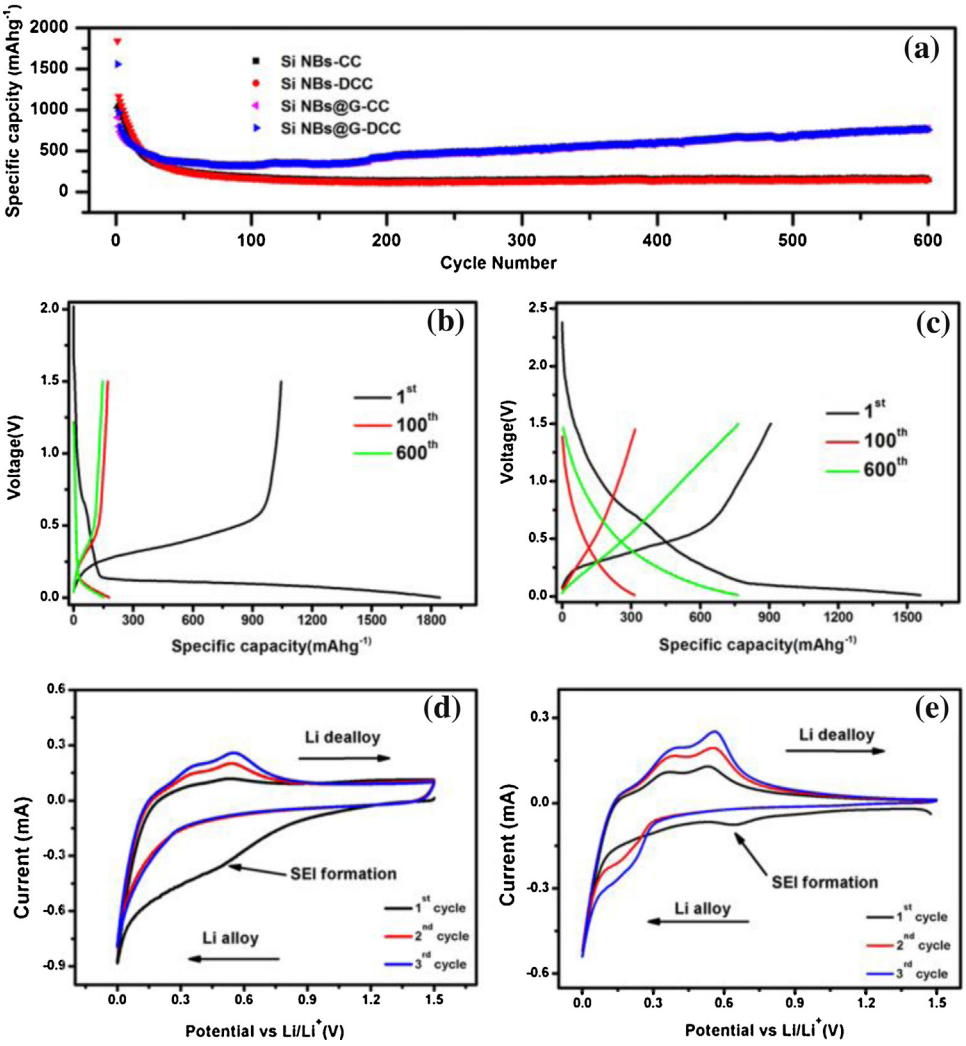

Fig. 4. (a) Electrochemical cycling results for Si NBs electrode and Si NBs@G electrode. The first DCC and CC for Si NBs electrode were 1844 and 1044 mAh g^{-1}, respectively. For the Si NBs@G, the first DCC and CCs were 1558 and 906 mAh g^{-1}, respectively. (b) Voltage profiles plotted for the first, 100th, 600th cycles for Si NBs electrode and (c) for Si NBs@G electrode. The capacity of Si NBs@G electrode gradually increased after 100 cycles. (d) Cyclic voltammetry curves for Si NBs and (e) Si NBs@G electrode. A broad reduction process between 0.1–0.3 V (vs. Li/Li+) on the charging curve refers to the Li-alloying process. The two oxidation peaks, located between 0.38 and 0.60 V, are assigned to the Li-dealloying process.

a totally amorphous structure (Li_xSi) with a thin SEI shell after the 10th cycle, indicating sufficient lithiation during cycling (Fig. 6(c) and (d)). Fig. 7(a) shows the TEM image of Si NBs@G after 600th cycle. At this stage, the anode material is mainly composed of congregated crystallites coated with thin amorphous SEI layer. The electron diffraction analysis indicates that the crystallites are a Li-rich phase $Li_{15}Si_4$. Electron energy loss spectroscopy (EELS) analysis of Li-alloying product Li_xSi in samples after 10th and 600th cycle shows the formation of alloys with increasing amount of Li after more cycles (see Fig. S1). This suggests an improved lithiation process of Si, hence enhancement of capacity. It can be seen that the thickness of SEI layers did not increase much during succeeding cycles (see Fig. 6(c) and Fig. 7(a)). Thus, a stable SEI membrane could be formed in graphene coated Si NBs, which further serves as a protecting layer for $Li_{15}Si_4$ crystallites. On the contrary, the Si NBs sample after 600th cycle is composed of discrete $Li_{15}Si_4$ particles covered with thick amorphous SEI layer (Supporting information, Fig. S2). Apparently, both thick SEI layer (which would cause higher irreversible capacity) and the fragmentation of Si NBs would lower the capacity.

4. Conclusions

The present study undertakes a promising strategy to improve the structural sustainability of Si NBs anode materials for Li-ions batteries via coating with graphene layers. The Si NBs have a diameter of around 200 nm and a thickness about 80 nm and the tube walls are composed of Si nanocrystals with a size about several nanometers. The obtained Si NBs@G anode demonstrated a gradually increasing capacity to ~765 mAh g^{-1} after 600 cycles, which is about 5 times the capacity of Si NBs anode without graphene coating. Detailed structural characterization clearly visualizes enhanced lithiation process in Si NBs@G that increases the effective mass of Si active materials along with prevention from pulverization of Si NBs owing to the protective coating of graphene. Meanwhile, formation of aggregated Li-rich $Li_{15}Si_4$ crystallites confined in the graphene layers provides additional lithiation/delithiation processes that lead to unexpected increase in capacity at later periods of cycling.

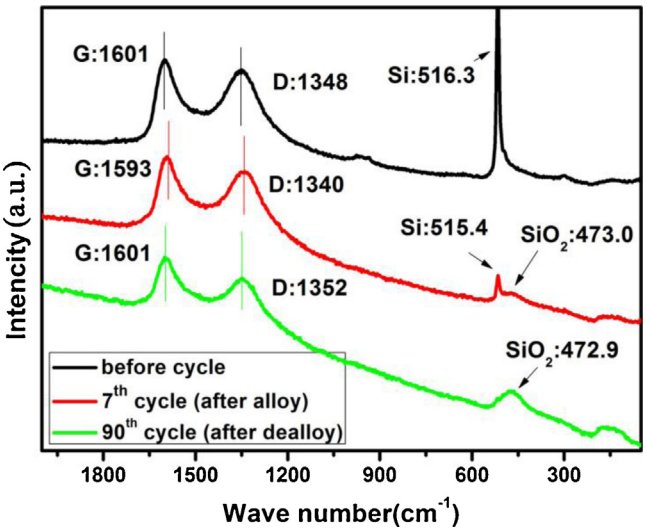

Fig. 5. Raman spectrum of Si NBs@G before and after its 7th (in alloy state), 90th (in dealloy state) cycle, respectively. The sharp peak of crystallized silicon finally disappears after the 90th cycle. (For interpretation of the references to colour in the text, the reader is referred to the web version of this article.)

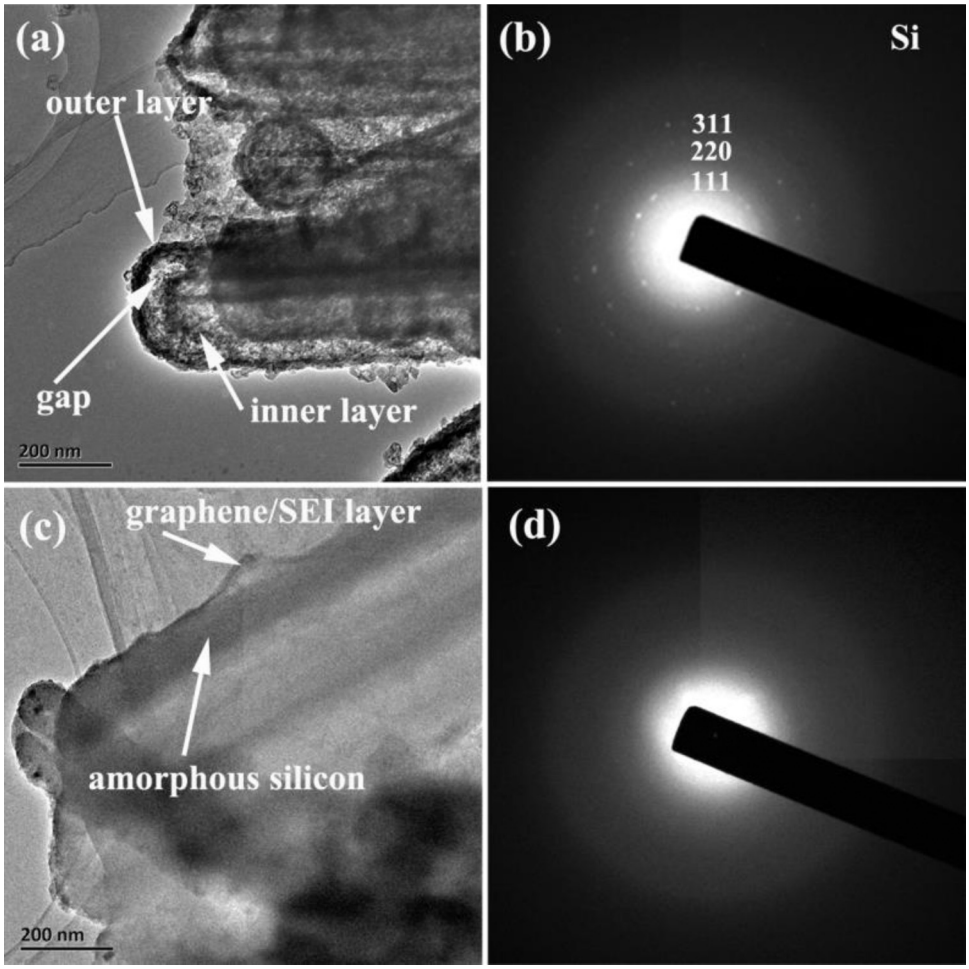

Fig. 6. TEM image of Si NBs after 10th cycle (after alloying) (a) and its diffraction pattern (b); TEM image of Si NBs@G after 10th cycle (after alloying) (c) and its diffraction pattern (d). Si NBs samples exhibit specific double-shell tubular morphology.

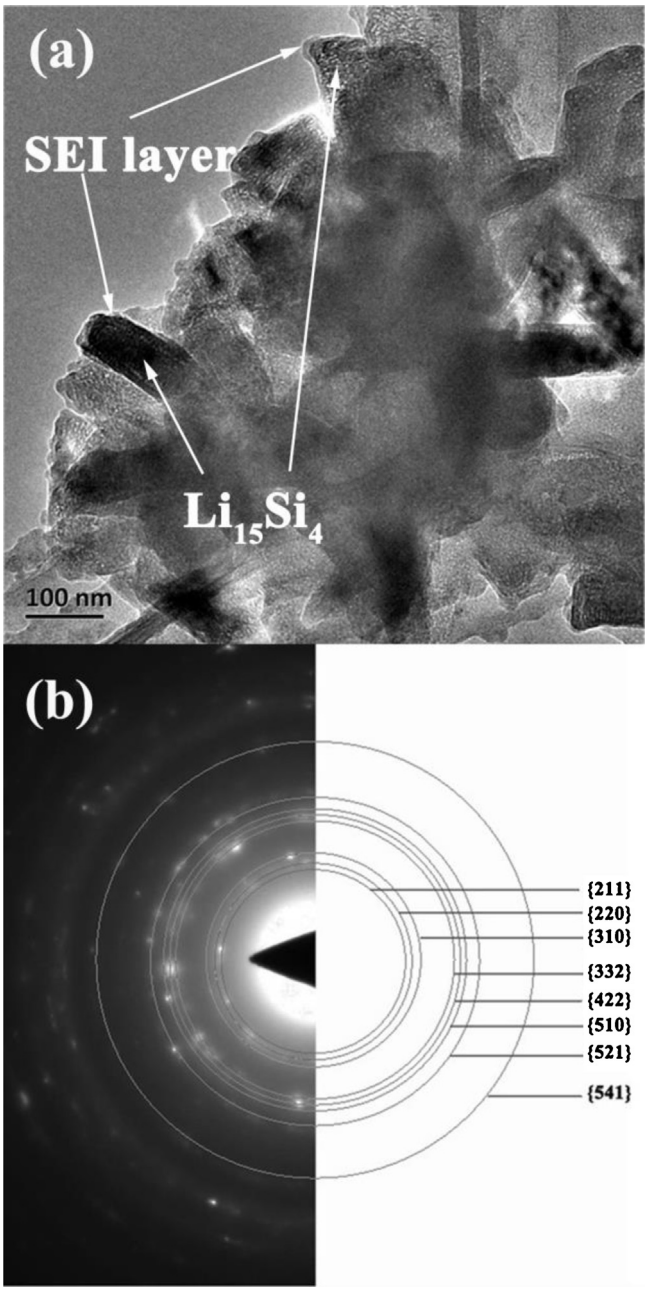

Fig. 7. TEM image of Si NBs@G after 600th cycle (after alloying) (a) and its SAED pattern (b). Fig. 7(b) indicates that the congregated crystallites in Si NBs@G after its 600th cycle are a Li-rich phase $Li_{15}Si_4$.

Acknowledgements

This work is supported by National Natural Science Foundation of China (NSFC) under the No. 51272270 and 61327811; the CAS/SAFEA International Partnership Program for Creative Research Teams; Shanghai Technical Platform for Testing and Characterization on Inorganic Materials (14DZ2292900); and Key Innovation Foundation of SICCAS.

Appendix A. Supplementary data

Supplementary data associated with this article can be found, in the online version, at http://dx.doi.org/10.1016/j.materresbull.2015.09.028.

References

[1] M.R. Palacin, Chem. Soc. Rev. 38 (2009) 2565–2575.
[2] H. Wu, Y. Cui, Nano Today 7 (2012) 414–429.
[3] B.A. Boukamp, G.C. Lesh, R.A. Huggins, J. Electrochem. Soc. 128 (1981) 725–729.
[4] N. Takami, A. Satoh, M. Hara, I. Ohsaki, J. Electrochem. Soc. 142 (1995) 371–379.
[5] Y. Zhu, W. Liu, X. Zhang, J. He, J. Chen, Y. Wang, T. Cao, Langmuir 29 (2012) 744–749.
[6] K. Fridman, R. Sharabi, E. Markevich, R. Elazari, G. Salitra, G. Gershinsky, D. Aurbach, J. Lampert, M. Schulz-Dobrick, ECS Electrochem. Lett. 2 (2013) A84–A87.
[7] W.L. Xu, J.C. Flake, J. Electrochem. Soc. 157 (2010) A41–A45.
[8] Z.H. Wen, G.H. Lu, S. Mao, H. Kim, S.M. Cui, K.H. Yu, X.K. Huang, P.T. Hurley, O. Mao, J.H. Chen, Electrochem. Commun. 29 (2013) 67–70.
[9] X.S. Zhou, A.M. Cao, L.J. Wan, Y.G. Guo, J. Nano Res. 5 (2012) 845–853.
[10] J. Bae, J. Solid State Chem. 184 (2011) 1749–1755.
[11] J. Chen, M. Liu, J. Sun, F. Xu, RSC Adv. 4 (2014) 40951–40957.
[12] Z.H. Bao, M.R. Weatherspoon, S. Shian, Y. Cai, P.D. Graham, S.M. Allan, G. Ahmad, M.B. Dickerson, B.C. Church, Z.T. Kang, H.W. Abernathy, C.J. Summers, M.L. Liu, K.H. Sandhage, Nature 446 (2007) 172–175.
[13] H. Wu, G. Chan, J.W. Choi, I. Ryu, Y. Yao, M.T. McDowell, S.W. Lee, A. Jackson, Y. Yang, L.B. Hu, Y. Cui, Nat. Nanotechnol. 7 (2012) 309–314.
[14] W.S. Hummers, R.E. Offeman, J. Am. Chem. Soc. 80 (1958) 1339.
[15] Y.H. Zhu, W. Liu, X.Y. Zhang, J.C. He, J.T. Chen, Y.P. Wang, T.B. Cao, Langmuir 29 (2013) 744–749.
[16] K. Meng, H.J. Guo, Z.X. Wang, X.H. Li, M.R. Su, B. Huang, Q.Y. Hu, W.J. Peng, Powder Technol. 254 (2014) 403–406.
[17] J.W. Wang, Y. He, F. Fan, X.H. Liu, S. Xia, Y. Liu, C.T. Harris, H. Li, J.Y. Huang, S.X. Mao, T. Zhu, Nano lett. 13 (2013) 709–715.
[18] X. Li, Y. Zhong, M. Cai, M.P. Balogh, D. Wang, Y. Zhang, R. Li, X. Sun, Electrochim. Acta 89 (2013) 387–393.
[19] X. Xin, X. Yao, Y. Zhang, Z. Liu, X. Xu, J. Solid State Electrochem. 16 (2012) 2733–2738.
[20] H. Wu, G.Y. Zheng, N.A. Liu, T.J. Carney, Y. Yang, Y. Cui, Nano lett. 12 (2012) 904–909.
[21] Y. Yao, N. Liu, M.T. McDowell, M. Pasta, Y. Cui, Energy Environ. Sci. 5 (2012) 7927–7930.
[22] D.H. Ying Xiao, Huixin Chen, Zhengliang Gong, Yong Yang, ACS Appl. Mater. Interfaces 5 (2013) 1681–1687.
[23] J.E. Trevey, K.W. Rason, C.R. Stoldt, S.H. Lee, Electrochem. Solid-State Lett. 13 (2010) A154–A157.
[24] J.R. Szczech, S. Jin, Energy Environ. Sci. 4 (2011) 56–72.
[25] X.H. Liu, L.Q. Zhang, L. Zhong, Y. Liu, H. Zheng, J.W. Wang, J.H. Cho, S.A. Dayeh, S. T. Picraux, J.P. Sullivan, S.X. Mao, Z.Z. Ye, J.Y. Huang, Nano lett. 11 (2011) 2251–2258.
[26] J.W. Wang, X.H. Liu, K.J. Zhao, A. Palmer, E. Patten, D. Burton, S.X. Mao, Z.G. Suo, J.Y. Huang, Acs Nano 6 (2012) 9158–9167.